GPPF-2017-18

EXPLOITING MODERN IMAGE PROCESSING IN SURFACE FLOW VISUALISATION

Tarek I. Abdelsalam
The British University in Egypt
tarek.ihab@bue.edu.eg
Sherouk, Cairo, Egypt

Richard Williams
Durham University
r.j.williams5@durham.ac.uk
Durham, United Kingdom

Grant Ingram
Durham University
g.l.ingram@durham.ac.uk
Durham, United Kingdom

ABSTRACT

Surface flow visualisation is an experimental technique where the surface of interest is painted with an oil and dye mixture before a flow is applied to the object. In regions of high shear stress the oil/dye mixture is then removed and in regions of low shear stress the oil/dye mixture stays or builds up. The resulting pattern can be analysed to determine the structure near the surface under test, this is normally done in a qualitative manner with flow structures being identified based on the expertise of the experimentalist.

Modern image processing tools can identify shapes and lines in pictures and this paper describes the development of an algorithm to apply these techniques to surface flow visualisation and derive quantitative numerical data from the visualisation images. The well know "Durham Cascade" a low speed, linear cascade with around 110 degrees of turning is used as a test case for this technique. The direction of streamlines, location of saddle points and positions of maximum shear stress were identified and quantitatively compared to computational fluid dynamics of the same case.

Overall this paper describes a process by which new information can be extracted from an existing and well used technique.

INTRODUCTION

Flow visualization is a general tool in fluid dynamics that aims to improve understanding of fluid flow behavior by translating physical characteristics into visible patterns, which can then either be qualitatively or quantitatively analyzed. Merzkirch [1] provides a modern overview of the topic. The key advantage of flow visualization techniques is their potential to provide information about entire flow fields compared to pressure probe measurements which are limited to discrete points.

Experimental flow visualization techniques have been a fundamental tool for studying flow patterns since Leonardo da Vinci's sketching of wake vortices downstream a bluff body in the fifteenth century. Merzkirch [2] has classified the experimental techniques into three main categories: addition of foreign materials, optical visualization, and field marking by energy. The first type is generally distinguished from the latter two by being an indirect way of visualizing the flow, since the visualized pattern is formed by the added material instead of the original fluid. The current research used the *Surface Flow Visualization* (SFV) by oil film, which belongs to the first category.

Surface Flow Visualization by Oil Film Technique

SFV by oil film has long been a standard technique for wind tunnel tests Maltby [3]. For turbomachinery applications, an advantage of this approach is its capability of visualizing corner flows that are rather challenging to access by non-intrusive optical visualization approaches.

Squire [4] presented an analytical model of an oil film and fluid interaction and concluded that the oil follows the boundary-layer surface streamlines except near separation and this deviation is more pronounced in laminar boundary layers.

The procedure involves coating the solid surface of interest by a viscous mixture of oil and colored dye. When exposed to the frictional forces applied by the flowing fluid, the mixture accumulates streaky pigment in the flow direction. The resulting deposition pattern is in the form of dried streaklines that provide information about the magnitudes and directions of velocity vectors near to the surface. The pattern can expose boundary layer features such as regions of flow transition from laminar to turbulent, and regions of flow separation and reattachment, which are displayed as diverging and converging streaklines, Bogdonoff [5]. Streaklines near separation regions can be particularly distinctive, since the skin friction is low enough to keep oil depositions for longer periods of time so accumulating more pigment. Although the pattern is usually recorded via a photograph taken immediately after the flow stops, some research studies have also reported the use of video to study the development stages of the streaklines.

The main limitation to this technique is the requirement for a mixture that is sufficiently viscous to hold on to the solid surface without running under the effect of gravity but also to form a pattern when subjected to the various magnitudes of shear stress encountered. It should also be volatile enough to entirely evaporate after the expiry of the steady flow conditions Merzkirch [6]. Accordingly; the composition of the mixture is dependent on the application and flow mode.

IMAGE PROCESSING IN FLUID MECHANICS

In terms of experimental fluid dynamics image processing tools have been predominantly used to analyze images produced from *Particle image velocimetry* (PIV) and optical flow visualization techniques, Hu et al [7]. For example in an attempt to develop a 3D particle tracking velocimetry by Laurent et al [8], a Python coded image processing programme was developed to spot the colors of tracers in polychromatic images of a PIV visualization.

Besides their extensive usage in medical ultrasonographic applications, Hough transformation methods are also used to detect and draw features in other medical applications, e.g. Carmo [9]. These methods are capable of detecting defective instances in images within certain shape classes, such as circles and lines, through a voting procedure. For example, air bubbles generated behind a micro‑orifice cavitation by a flowing oil were analyzed optically by Iben et al [10] with the aid of image processing tools. The flow was photographed and recorded by a digital camera, while the bubbles were detected by a MATLAB code based on the circular Hough transform method to determine their number and diameters.

Modern image processing tools can also be used for analyzing video sequences displaying the development of a flow features. For instance, they were used by Japee et al [11] to analyze several video recordings of red blood cell dynamics to track and study the oxygen conveyance in capillary networks. Although the method used was not capable of analyzing the entire capillary flow field individual red blood cells were reported to be sufficiently clear to extract useful and accurate information about their velocities.

Image processing tools were used by Pierce et al [12] to process images from video recordings of the development of flow features on a flat plate visualized by the SFV by oil film technique. Individual frames with clear fragments were then processed by PIV processing software. This processing algorithm consisted of two nonlinear filters: 'concentration' and 'subtraction sliding minimum'. The former was used to solve the smoothening effect of pigment over large areas of the images and the second filter was used to locate the local minimum intensities, within a user-defined length, to increase the contrast and convert the images into binary.

Overall, it is evident that sophisticated image processing algorithms are deployed routinely with good effect to obtain information about complex flow fields.

APPLICATIONS TO TURBOMACHINERY

The fluid dynamics of turbomachinery flows are complex but have been extensively researched. To select the example of axial turbine flows - the formation of secondary flows are described extensively by Sieverding [13] and Langston [14] and flows with a tip clearance have been described by Bindon [15]

In a recent study by Allan et al [16], the authors asserted that the existing numerical codes do not provide precise and reliable results about the boundary layer transition phenomena occurring in gas turbines. Their study on stream-wise vortex formation involved extensive manual analysis of SFV images to obtain quantitative results.

SFV by oil film and ink dots are the leading non-optical approaches used to explore the intricate 3D flow behavior in the turbine passage as emphasized by Ristić [17]. For instance, secondary flows occurring near the endwalls of a linear turbine cascade were visually examined by means of SFV with an oil-lampblack mixture as described by Sanitjai [18]. Qualitative descriptions of vortex behaviors were deduced from the patterns such as a strong passage vortex.

A seminal study was performed by Langston [19] to explore the characteristics of the endwall boundary layer by means of SFV by ink depositions on endwall and airfoil surfaces. SFV helped to qualitatively determine the location of flow separation relative to the saddle point at inlet boundary layer.

Both SFV by oil film and ink dots techniques were employed by Volino [20] to study the flow behavior near the endwall and suction side of a turbine blade. Both techniques revealed endwall flow features including the crossflow, saddle point, and migration route of the horseshoe vortex along the passage until its imposition on the suction side of the neighboring blade. The alcohol used in the ink dot method evaporated upon contacting the flow, which enabled the ink tracers to provide permanent record of the pattern after drying. The resulting patterns from both techniques qualitatively confirmed the location of the saddle point to be near to the leading edge of the pressure side of the blade, while roughly lying on a line linking the leading edges of the suction and pressure sides of two adjacent blades.

Holley [21] quantitatively investigated the contribution of endwall skin friction on the overall aerodynamic loss through skin friction measurement using oil film interferometry. The technique was used to estimate the skin friction coefficients and identify the directions of endwall shear forces. The outcomes from this study exposed a clear difference between the experiment and the CFD. The authors recommended future efforts should focus on developing experimental techniques to provide more detailed and comprehensive information about the endwall and airfoil skin frictions for more precise and reliable validation of CFD codes.

Flow visualization techniques have also been used to exhibit the benefits of newly proposed design improvements. In a study by Friedrichs et al [22], the effectiveness of an endwall adiabatic film-cooling was investigated with the aid of selected flow visualization techniques including SFV by oil film. Similarly, the SFV by oil film technique was used by Ingram [23] to highlight the benefits of using proposed endwall profiling designs on mitigating secondary flows.

As can been seen from the above survey despite the wide use of SFV in turbomachinery experimentation most images are analyzed based on the experimenters' expertise

and in a qualitative manner. This advance presented in this paper is that an algorithm using modern image processing tools is developed and used to extract quantitative information from SFV studies. These procedures were developed and applied on the well known "Durham Cascade".

IMAGE CAPTURE USING THE CASCADE

SFV images generated in previous campaigns were used to develop the algorithm but during the work it became apparent that these legacy images lacked crucial information so a short test campaign was conducted to capture new images. The algorithm is described in the following section but the process for obtaining photographs is described here.

The so-called "Durham Cascade", a low speed linear cascade of a high pressure turbine blade was used. This cascade has been extensively used for secondary flow research and for this paper was used with and without a tip clearance. The detailed design of the cascade is described by Bagshaw et al [24], and summarized in Table I.

TABLE I: Key Cascade Parameters

Inlet Flow Angle	42.75^0
Exit Blade Angle	-68.70^0
Blade Pitch	191 mm
Blade Axial Chord	181 mm
Tip Clearance of Casing Endwall	3.75 mm
Blade Span	375 mm
Reynolds Number	4×10^5
Turbulence Intensity	5%
Freestream Velocity	19.1 m/s
Dynamic Pressure	215 Pa

The endwall of the cascade was coated with a white matt melamine resin layer. A line parallel to the trailing edges was scribed on the endwall and highlighted with a dark blue pen to mark the axial reference axis. This line was 45 mm downstream from the trailing edges. The tangential projection of one of the trailing edges on the scribed line was marked as an origin point O, while the trailing edge point itself was denoted as O_{TE}, but was not marked on the endwall. After finishing the experiment, a 7 by 7 chessboard pattern was glued on the endwall before photographing for calibration purposes. For precise alignment of that pattern with the reference line, a parallel line was marked out at 70 mm to enclose the printed pattern from both sides as illustrated in Fig 1. The pattern also formed the axial reference axis and the scale on both axes, as each chessboard square was 10 mm by 10 mm.

A mixture of paraffin and red colored, UV fluorescent, dye powder was prepared with a mixture ratio of 5.5 ml of paraffin to 1 ml of dye. This ratio was set by trial and error to ensure that the mixture revealed flow features at the full range of shear flows. The mixture was applied uniformly on the center of the endwall covering at least the middle two cascade passages. The mixture was applied by paintbrush perpendicular to the anticipated flow direction so that any remaining brush marks were obvious.
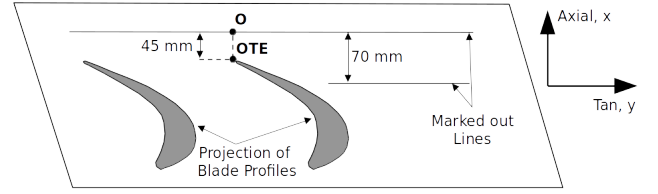

Fig 1: Pre-experiment marking out and location of the reference point O. (Not to scale)

Two runs were performed at the specified operating conditions: one with a tip clearance of 3.75 mm, representing a "casing" endwall case, and another with a zero tip clearance to represent a "hub" endwall case. The operating conditions were maintained for 10 minutes before removing the endwall for photography.

Images of 2992 pixels by 2000 pixels were created by a 'Nikon D3300 DSLR' camera fitted with a 'AF-S Nikkor 18-55mm' lens with aspherical lens elements, which moderate optical distortions such as spherical aberration and astigmatism. The aperture size was set as f/6.3 for input images to the streaklines detection algorithm and saddle point procedure, while a narrower aperture of f/13 was used for input images to the maximum wall shear point detection procedure. The camera was attached to a horizontal tripod arm, while the endwall was laid flat for image capture.

Different light conditions were tested but the indoor fluorescent ambient light coupled with an incident UV were found to be the best for the streakline detection algorithm. Additional uniformly distributed lights were used for input images to the maximum wall shear detection algorithm in an attempt to eliminate the camera and tripod shading by evenly distributing the illumination all over the endwall surface. Twenty photos were then taken per run at different camera orientations, in addition to a perpendicular, which was used as the base input to the algorithm.

For comparison, a pre-existing RANS CFD solution of the cascade with and without tip clearance was used. This solution used 1.7 million cells, was computed using Fluent 14 and used the enhanced wall treatment with a k-epsilon turbulence model.

IMAGE PROCESSING ALGORITHM

The resulting images were then processed through a multi-stage "Python" computer program using functions from an off-shelf, open source computer vision library module named OpenCV 3.0. Some auxiliary functions were obtained from other modules such as Numpy, SciPy, Matplotlib, etc. The main stages of the developed algorithm for streakline detection are shown in Fig. 2. Further details including all the equations used in the algorithm are found in Abdelsalam [25] and the software used for this paper is available on-line at the URL given for Abdelsalam [25].

Calibration and Tilt Correction

An initial calibration stage was used (Green box in Fig. 2) to alleviate the radial and tangential distortions caused by intrinsic properties of the camera lens. Such properties are characteristically fixed for the same lens, so they were modeled as constant parameters that can be evaluated by

Fig. 2. Flow chart of streakline detection algorithm.

solving a sufficient number of equations, at least equal to the number of unknown parameters. OpenCV calibration functions follow a model developed by Zhang [26], where each equation is generated from a snapshot of a defined planar pattern of 'object points' with a different orientation. The 6x6 square corners of the selected 7x7 chessboard pattern were used as the object points with their known horizontal and vertical spacings of 10 mm.

This calibration procedure was tested by calibrating an image of two successive blade profiles scribed on the endwall with marked out trailing edges. The chessboard pattern was used to estimate the 191 mm pitch between the two marked out points by multiplying the 10 mm chessboard square spacing by the probed pitch, in pixels, divided by the square spacing in pixels. The pixel coordinates were probed by an OpenCV mouse click function. This was repeated for the uncalibrated image. The percentage error in the pitch estimation was found to drop from 3.29% to 0.11% of the pitch after applying the calibration algorithm with twenty images at different orientations. This procedure was applied to all visualization images, which led to the visually observable correction shown in Fig. 3. All computed coordinates were corrected in both directions by applying basic trigonometric relations.

Preprocessing Stages

The next stages (Red boxes in Fig. 2) were characterized as preprocessing stages. Firstly the calibrated visualization images were divided into rows and columns of a user-defined number/size of rectangular cells followed by a grayscale conversion stage. The number and size of cells are critical factors affecting the detection accuracy of the algorithm, as curved streaks require smaller cells to align, while smaller cells can miss out sections of a streakline. Since each cell had its own local origin as an independent minor image, all local cell coordinates required transformation back to the global system.

Fig. 3. Input image calibration. Left: Before calibration. Right: After calibration.

Reduction of image noise was then performed on each cell using a selected low-pass filter. Several methods of low-pass filtering were tested on sample images including Averaging, Median, Gaussian, and Bilateral filtering. The Bilateral filter was found to be the best in preserving streakline edges from being blurred. However, its filtering process was the slowest and, in some cases, it created a few falsified edges.

The key advantage of the Bilateral filter over usual Gaussian filters used in the literature is its inclusion of an additional Gaussian-based weighted average filtering component that depends on intensity differences between neighboring pixels, whereas conventional Gaussian filters depend only on their Euclidean distances. Therefore, neighboring pixels, determined by an input space sigma σ_s, with closer intensity values, determined by an input color sigma σ_c, can only influence the smoothening value of the tested center pixel as explained by Paris et al [27]. Sizes of the two sigmas were set by trial and error for each visualization image depending on the level of Gaussian noise.

A high-pass filter was then applied to expose the intensity gradients in each cell. The process was a weighted, with a selected kernel, differentiation of a sampled intensity function to find the directions of increasing, or decreasing, pixel values.

The derivative functions can either be of first degree, *Sobel* derivatives, or second degree, *Laplacian* derivatives. Therefore, a Sobel operator can be applied for a certain general direction, vertically (V) or horizontally (H), while a Laplacian operator is, by definition, functioning in both directions. After testing the two operators, it was found that a Sobel operator applied closely in line with the streaklines was more accurate in the detection than the Laplacian. However, the single direction Sobel operator failed to detect most of the curved streaklines near to the leading edge. This problem was substantially solved, by superimposing two image convolution operations using horizontal and vertical Sobel kernels.

Canny Edge Detection and Linear Hough Transform

After finding the intensity gradients and their directions for each cell the core of the image processing algorithm was run (Blue boxes in Fig. 2). Edges were detected using a *Canny* edge detection function. The function starts with a

non-maximum suppression step, which was applied to get rid of pixels that may not form an edge; instead, they usually surround, and so thicken, the edges. This step was done by checking every pixel if it possesses a local intensity maximum within its neighbor pixels along the gradient direction. If a pixel had a local intensity maximum, it was considered to lie on an edge perpendicular to that gradient direction; otherwise, it was suppressed.

The subsequent step was to remove edge pixels with weak gradients, caused by color variation, by *hysteresis thresholding*. At this step, a maximum and minimum intensity values were assigned to form an intensity range for suspected edge pixels. Pixels with higher intensity values than the maximum limit were taken as definite edge pixels, while those with lower values than the minimum limit were suppressed and considered as definite non-edge pixels. Pixels with intensity values between the limits were tested based on their connectivity with their neighboring pixels. Accordingly, if a pixel with a value within the range and had a neighborhood of definite edge pixels, it was taken as an edge pixel and vice versa.

When testing the effect of assigned hysteresis limits on detected edges in the visualization images, it was generally observed that narrower limits helped avoid the detection of noisy edges, but they tended to overlook streaklines at high shear (pale regions) such as downstream of the trailing edges due to reduced edge gradient values.

The next algorithmic stage was the *Linear Hough Transform*, which was used to detect and draw conforming lines on the detected edges in each cell to resemble the velocity vectors. Lines were detected and drawn based on the Hesse normal form of the straight line equation, since the Cartesian form is problematic for vertical lines due to their infinite slopes. Therefore, each line was represented by polar coordinates based on the local cell coordinate system.

The lines were detected following a voting procedure, which depends on the lengths of detected edges in the cells, using a 2D accumulator array. Regarding the detection accuracy, the selected increments for the rows and columns were 1 pixel and $\pi/180$, respectively. This accumulator counted the instances of possible existence of straight lines at each pixel, so that it incremented the number of *votes* of a certain straight line by one if the tested pixel was located on that line. Based on an assigned *Voting Threshold* value, lines with a number of votes greater than or equal to that value are drawn in the cell.

Before transforming their local cell coordinates into image coordinates, the returned polar coordinates were first transformed into Cartesian coordinates.

All previous stages were repeated for each individual cell covering the entire image, while returning the vectors positions and angles relative to the image coordinate system.

Secondary Procedures for Locating Points of Interest

Since the background color of endwall surface was white, the maximum wall shear point was located by an OpenCV function that locates the pixel with the highest intensity value in a grayscale image. To evade disruptions from unbrushed white spots, or any other source of salt and pepper noise pixels, a pre-processing 15 by 15 median low-pass filter was included. Application of this procedure on the zero tip clearance case was difficult, since it always located the dye-free blade profile region. Therefore, all blade profiles in the image were brushed with a dark paint after finalizing the experimental run. Suppression of blade profile pixels would be a more elegant solution but the adopted approach provides a proof of concept of the technique.

The positional coordinates of the saddle point and the origin point O were acquired from each calibrated visualization image using the OpenCV mouse click function. Probing the saddle point location was done after all velocity vectors were drawn on the image.

Comparisons with CFD and Direct Measurement

In order to provide comparable results with the CFD solution, the Euclidean origin was unified as the trailing edge of the blade. Hence, the coordinates of the point O_{TE} were obtained from point O, in each image, by adding the equivalent pixel value of 45 mm in the axial direction. After correcting the tilted image coordinates pixel units were then converted into metric units. Both these conversions used data from the chessboard calibration stage. The converted metric coordinates were then used to probe corresponding features in the CFD solution by using ANSYS CFD-Post. Due to the no slip condition in the CFD solution, velocity data was obtained at 0.1 mm above the endwall surface.

Locations of the saddle points at the casing and hub endwalls were further validated by physical measurements of their positional coordinates using two perpendicular rulers.

RESULTS AND DISCUSSION

The lines detected in the flow visualisation images with a voting threshold of 18 and a 3.75mm tip clearance is shown in Fig. 4. The accurate location of the visualisation image allows the blade profiles to be plotted directly on the image. The effect of using higher and lower voting threshold values of linear Hough transform on the detected streaklines is exhibited in Fig 5 by showing a higher threshold value of 20. With a higher threshold value, the algorithm tended to be more conservative with the streaklines detection, and so providing less information per unit area. In contrary, lower thresholding allowed the algorithm to result in more lines per unit area, but it seemed to create more horizontal, vertical, and diagonal noise vectors scattered around the image, which can be controlled, though not eliminated, by slightly narrowing the hysteresis limits of the Canny operator. All quantitative results in this paper use a voting threshold of 18.

Angles of twenty five, randomly selected and dispersed, detected lines were compared with their corresponding values in the CFD solution. Since the alogrithm currently detects lines these could correspond to velocity vectors that could be 180^0 apart (e.g. up or down in Fig 4) so for the current comparison the user had to make a judgement as to which direction the flow was travelling. The average absolute deviation between the two solutions was 2.2^0 with a maximum of 4.1^0.
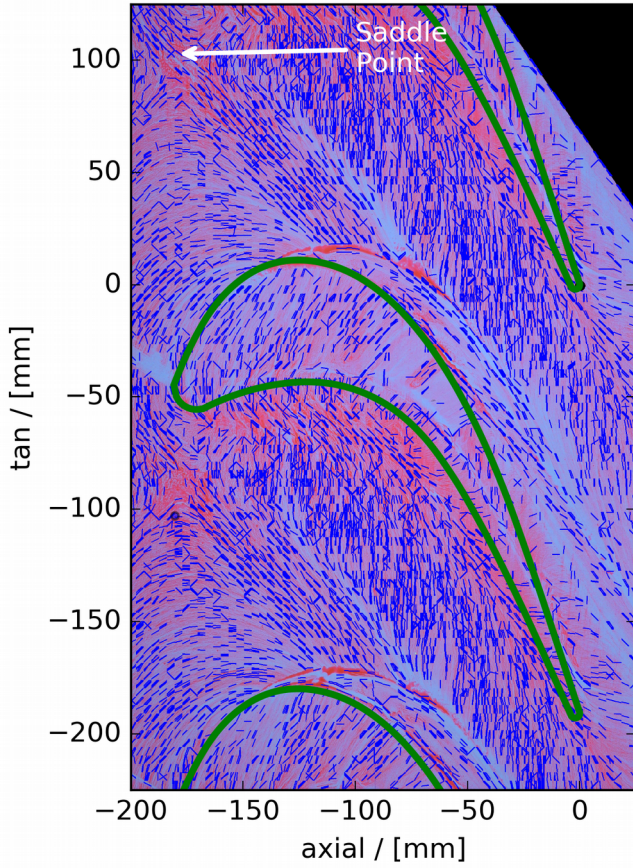
Fig. 4. Image processing solution for tip clearance (with voting threshold of 18).
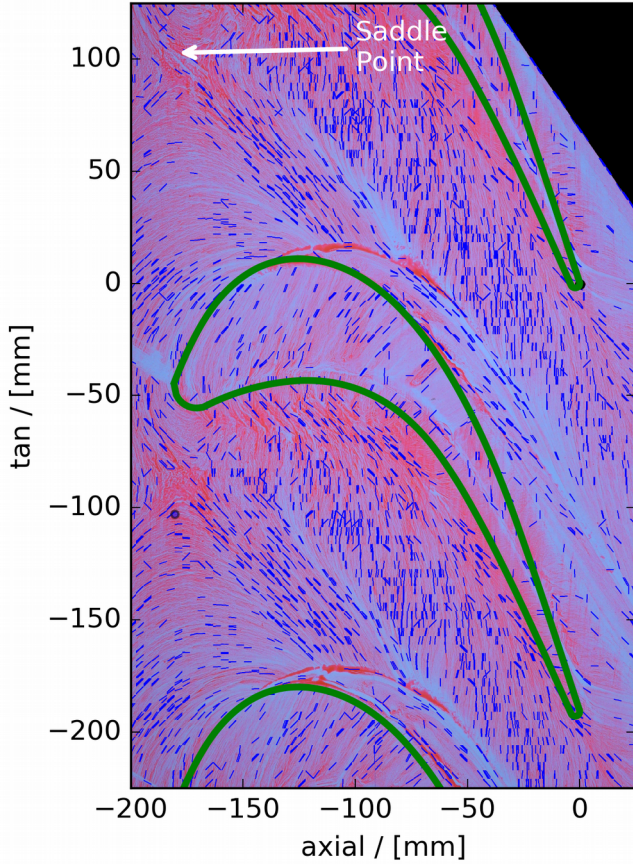

Fig. 5. Image processing solution for tip clearance (with voting threshold of 20).

This result is encouraging but it is an open question as to whether the differences are down to modelling errors in the CFD or image processing errors thrown up in the present algorithm. To resolve this issue some form of generated flow visualisation image with known angles would need to be processed by the algorithm and this is the subject of ongoing work. The key point is that quantified comparisons of SFV and CFD are able to be generated.

The evaluated positional coordinates of the saddle point from the two solutions were compared relative to the measured coordinates for the two tip clearance cases as shown in Table III and also annotated in Figs 4 and 5.

TABLE III
Saddle Point Results

Clearance (mm)	Solution Method	Position		Deviation	
		Axial / (mm)	Tan / (mm)	Axial /(mm)	Tan / (mm)
3.75 (Casing)	Ruler	-180.25	103.00	Reference	
	Image Proc.	-180.56	102.81	0.31	0.19
	CFD	-184.35	122.57	**4.10**	**19.57**
Zero (Hub)	Ruler	-186.00	87.00	Reference	
	Image Proc.	-185.81	86.55	0.19	0.45
	CFD	-188.77	113.49	**2.77**	**26.49**

As indicated from the tabulated results, the deviation of the saddle point estimated from the CFD solution can be quantified in both directions, by using the extracted image processing results as the reference. Deviations between the ruler measurements and image processing results are within the acceptable limit, noting that ruler measurements have a precision of ± 0.5 mm. Such deviations between the location of flow features in CFD and experiments are also found in the wider literature (e.g. Holley [21] or Ingram [23]), the advance here is that they can be easily and more accurately quantified.

TABLE IV
Maximum Wall Shear Point Results

Clearance (mm)	Solution Method	Position		Deviation	
		Axial / (mm)	Tan / (mm)	Axial /(mm)	Tan / (mm)
3.75 (Casing)	Image Proc.	-40.41	-33.56	Reference	
	CFD	-67.58	-67.57	**27.17**	**-34.01**
Zero (Hub)	Image Proc.	-70.06	3.39	Reference	
	CFD	-61.11	-6.86	**-8.95**	**-10.25**

Similarly, evaluated coordinates of the maximum wall shear point from both approaches are tabulated in Table IV along with the deviation from the CFD value.

There is a large deviation between the location of the maximum shear points in the two cases. For the hub this is simply that the flow feature in question is located in a different position but with the same underlying behaviour. For the casing however Fig. 6 illustrates that the maximum wall shear stress in the CFD is under the tip clearance on the

pressure side of the blade, while the image processing instead refers to a point near to the suction side of the blade. Despite the dramatic differences apparent in Fig. 6 the flows are fundamentally similar: both feature a tip clearance vortex interacting with a passage vortex and separation within the tip gap. In this particular case the inlet boundary layer to the CFD was found to be set smaller than required due to a configuration error, accounting for some of the differences seen. However even a 1.7M cell CFD solution lacks the grid resolution required to resolve the detailed streaklines revealed by the oil and dye mixture seen in Fig. 6.
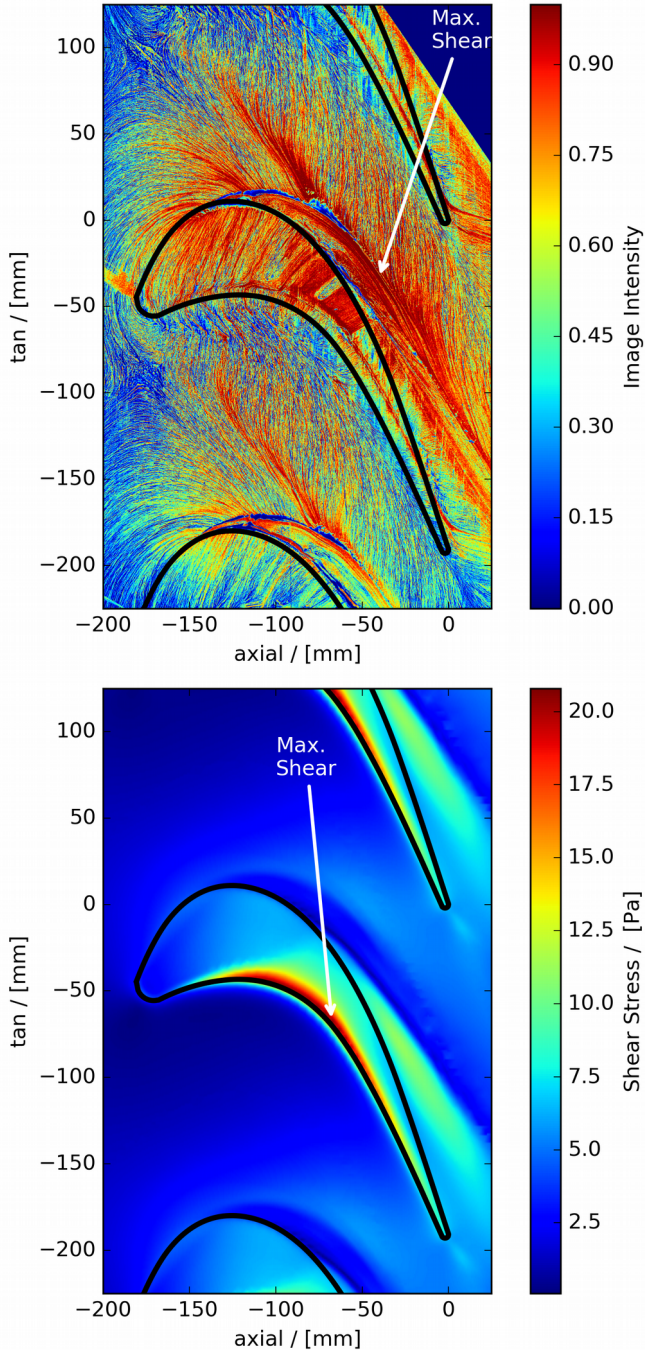
Fig. 6. Location of maximum wall shear point on the casing endwall. Top: Image processing with HSV color display. Bottom: CFD solution.

CONCLUSIONS

An image processing algorithm was developed to detect and extract data from endwall streaklines visualized by an oil film surface flow visualisation. The algorithm uses off-the-shelf software components. Secondary procedures were also developed to locate the saddle point and maximum wall shear point on the casing and hub endwalls although these rely heavily on user interaction.

Flow visualization images were generated using the "Durham Cascade" as a test case. The key feature of this image set is a chessboard calibration target which allows off-the-self image processing software to correct for lens distortion and therefore improve the location of features in the SFV image. These images and the software used in this paper are available for download.

The algorithm allows quantitative comparisons to be made between SFV and CFD. For the case study used in this paper the maximum difference in numerical and experimental flow angle was just above four degrees. The location of maximum wall shear point showed that the CFD used did not accurately replicate the nature of the flow in the tip gap. The CFD model predicted the maximum shear stress to occur under the blade tip but the experiment highlights that this occurs in the tip leakage vortex.

The main flaw in the algorithm is the formation of scattered noise vectors, which seemed to appear vertically, horizontally, or inclined at 45°. Nevertheless, these awkward vectors can easily be detected and excluded or they can be controlled by optimizing the thresholding levels.

Further development of the algorithm should include counting numbers of converging and diverging streaklines in selected regions. It will also be necessary to generate some form of "calibration target" for the streakline algorithm to quantify errors in the image processing algorithm. The current approach of examining differences between the CFD and experiment leaves open the question whether the CFD is wrong or the image processing algorithm is producing spurious results.

However, the work presented here has successfully described the use of some standard image processing procedures for extracting quantitative data from surface flow visualisation. The authors hope that these techniques will become routine when using SFV in turbomachinery applications.

NOMENCLATURE

SFV	Surface flow visualisation
O	image origin point
O_{TE}	trailing edge origin point
x,y	axial and tangential coordinates

ACKNOWLEDGMENTS

REFERENCES

[1] W. Merzkirch, "Flow visualization," in *Springer handbook of experimental fluid mechanics*, Berlin, Springer Berlin Heidelberg, 2007, pp. 857-870.

[2] W. Merzkirch, "Principles of flow visualization," in *Flow visualization*, 2nd ed., New York, Academic Press, Inc., 1987, pp. 1-4.

[3] R. L. Maltby, "Smoke techniques for use in low speed wind," in *Flow visualization in wind tunnels using indicators*, AGARDograph No. 70, 1962, pp. 87-109.

[4] L. C. Squire, "The motion of a thin oil sheet under the boundary layer on a body," *Journal of Fluid Mechanics*, vol. 11, no. 2, pp. 161-179, 1961.

[5] S. M. Bogdonoff, "Some observations of three-dimensional shock-wave/turbulent boundary-layer interactions," in *Turbulent shear-layer/shock-wave interactions*, Palaiseau, Springer Science & Business Media, 2013, pp. 261-272.

[6] W. Merzkirch, "Oil film visualization," in *Techniques of flow visualization*, Neuilly-sur-Seine, AGARD, 1987, pp. 2-5.

[7] B. Hu, W. Cheng, L. Zhou and W. Cheng, "Research of image processing technique in flow visualization," in *Advances in Water Resources and Hydraulic Engineering*, Nanjing, Springer International, 2008, pp. 1934-1939.

[8] K. Laurent, M. Barthès, V. Lepiller and Y. Bailly, "Development of a 3D Particle Tracking Velocimetry method and its associated Python-coded software for image processing," in *10th Pacific Symposium on Flow Visualization and Image Processing*, Naples, 2015.

[9] B. S. Carmo, "Image processing in echography and MRI," Ph.D. dissertation, Dept. Electron. Eng., Southampton Univ., Southampton, 2005.

[10] U. Iben, F. Wolf, H. Freudigmann and J. Fröhlich, "Optical measurements of gas bubbles in oil behind a cavitating micro-orifice flow," *Experiments in Fluids*, vol. 56, no. 6, p. 114, 2015.

[11] S. A. Japee, C. G. Ellis and R. N. Pittman, "Flow visualization tools for image analysis of capillary networks," *Microcirculation*, vol. 11, no. 1, pp. 39-54, 2004.

[12] A. J. Pierce, F. K. Lu, D. S. Bryant and Y. Shih, "New developments in surface oil flow visualization," in *27th AIAA Aerodynamic Measurement Technology and Ground Testing Conference*, Chicago, Illinois, 2010.

[13] C. H. Sieverding, "Recent progress in the understanding of basic aspects of secondary flows in turbine blade passages," *Journal of Engineering for Gas Turbines and Power*, vol. 107, no. 2, pp. 248-257, 1985.

[14] L. Langston, "Secondary flows in axial turbines—a review," *Annals of the New York Academy of Sciences*, vol. 934, no. 1, pp. 11-26, 2001.

[15] J. P. Bindon, "The Measurement and Formation of Tip Clearance Loss," *Journal of Turbomachinery*, vol. 111, no. 3, pp. 257-263, 1989.

[16] W. D. E. Allan, J. P. Gostelow and S. I. Hogg, "Experimental study of stream-wise votex formation on swept circular cylinders in cross-flow," in *ASME Turbo Expo 2015: Turbine Technical Conference and Exposition*, Montréal, 2015.

[17] S. Ristić, "Flow visualisation techniques in wind tunnels: part I – non optical methods," *Scientific Technical Review*, vol. 57, no. 1, pp. 39-50, 2007.

[18] S. Sanitjai, "Flow visualization of secondary flow near blade/endwall region in a linear turbine cascade," in *17th Conference on Mechanical Engineering Network of Thailand*, Bangkok, 2003.

[19] L. S. Langston, M. L. Nice and R. M. Hooper, "Three-dimensional flow within a turbine cascade passage," *Journal of Engineering for Power*, vol. 99, no. 1, pp. 21-28, 1977.

[20] R. J. Volino and K. A. Flack, "Surface flow visualization of a scaled-up turbine blade passage," *Measurement Science and Technology*, vol. 11, no. 7, p. 987–991, 2000.

[21] B. M. Holley, S. Becz and L. S. Langston, "Measurement and calculation of turbine cascade endwall pressure and shear stress," *Journal of Turbomachinery*, vol. 128, no. 2, pp. 232-239, 2006.

[22] S. Friedrichs, H. P. Hodson and W. N. Dawes, "The Design of an Improved Endwall Film-Cooling Configuration," *Journal of Turbomachinery*, vol. 121, no. 4, pp. 772-780, 1999.

[23] G. L. Ingram, "Endwall profiling for the reduction of secondary flow in turbines," Ph.D. dissertation, Dept. Eng., Durham Univ., Durham, 2003.

[24] G. I. a. D. G.-S. David Bagshaw, "A turbine cascade facility for secondary flow research, GT2006-90868," in *ASME Turbo-Expo 2006*, Barcelona, 2006.

[25] T. I. Abdelsalam, "Exploiting Modern Image Processing in Surface," Durham University, MSc Report, Durham, 2016. Software at: http://community.dur.ac.uk/g.l.ingram/download.php

[26] Z. Zhang, "A flexible new technique for camera calibration," *IEEE Transactions on Pattern Analysis and Machine Intelligence*, vol. 22, no. 11, p. 1330–1334, 2000.

[27] S. Paris, P. Kornprobst, J. Tumblin and F. Durand, "From Gaussian convolution to Bilateral filtering," in *Bilateral filtering: theory and applications*, Paris, Foundations and Trends, 2009, pp. 4-10.

[28] L. Hesselink, "Digital image processing in flow visualization," *Annual Review of Fluid Mechanics*, vol. 20, no. 1, pp. 421-486, 2003.

[29] C. Hah, "A Navier-Stokes analysis of three-dimensional turbulent flows inside turbine blade rows at design and off-design conditions," *Journal of Engineering for Gas Turbines and Power*, vol. 106, no. 2, p. 421–429, 1984.